Supporting Information for

Ocean bottom distributed acoustic sensing for *T*-wave detection and seismic ocean thermometry

Zhichao Shen[1] and Wenbo Wu[1]

[1]Department of Geology and Geophysics, Woods Hole Oceanographic Institution, Woods Hole, MA, USA

Contents of this file

Text S1 to S6
Figures S1 to S10
Tables S1

Text S1. Earthquake origin time, location, and magnitude of NEPTUNE *T*-wave catalog

To determine the origin times and locations of earthquakes in the NEPTUNE *T*-wave catalog, we perform a grid search by minimizing the misfit function $\psi = \sum_{i=1}^{n} |t_i^{predict} + t^{origin} - t_i^{pick}|$, where n is the number of stations used for grid search. The origin time t^{origin} is calculated as $t^{origin} = \frac{1}{n}\sum_{i=1}^{n}(t_i^{predict} - t_i^{pick})$, where $t_i^{predict}$ and t_i^{pick} denote the predicted and picked seismic arrival time at ith station, respectively. We use a global 1D model IASP91 to calculate the predicted arrivals (Kennett & Engdahl, 1991). For *P*-waves and *S*-waves, we manually pick up their onset times on the vertical seismograms in a frequency band of 5-10 Hz. The searched area is bounded by 47°N and 52°N in latitude and 126°W and 132°W in longitude with an interval of 0.02°. When *P*-waves and *S*-waves are not available, event locations are constrained by *T*-waves. The arrival times of *T*-waves are picked at their envelop peaks and the searched grids are limited to seismic active areas (Figure S1a).

When clear *P*-waves and *S*-waves are available, we compute the local magnitude given as $M_L = logA + \log\left(\frac{D}{100}\right) + 0.00301 * (D - 100) + 3.0$ (Hutton & Boore, 1987), where A is the peak-to-peak amplitude of Wood Anderson type seismograms and D represents the epicentral distance. We convert the waveforms to Wood Anderson seismograph, filter them to 2-10 Hz, calculate the peak-to-peak amplitude and then compute the local magnitude by averaging over the three components of all available stations.

Text S2. *T*-wave travel time sensitivity kernel

We use the 2D spectral element method SPECFEM2D (Komatitsch & Tromp, 1999) to compute the *T*-wave travel time sensitivity kernels. Following Wu et al. (2023), we incorporate the global sediment and real bathymetry features to build a 3230 km (distance) X 40 km (depth) 2D slice model. A very shallow sea mountain present on the source-receiver great circle path seriously blocks the *T*-wave propagation, so we take another path, which corresponds to an effective source at 80 km further west, to avoid the strong blocking effects. The ocean sound speeds are calculated using the GSW package (McDougall & Barker, 2011) with the temperature and salinity inputs from the ECCOv4r4 climatology (Forget et al., 2015). The model is meshed with 20,000 (distance) X 96 (depth) elements to resolve 3.5 Hz *T*-wave. We cut the synthetic *T*-wave with a 60 s time window and run adjoint simulations to calculate the *T*-wave travel time sensitivity kernels (Figure S4).

Text S3. *T*-wave amplitude ratio between NEPTUNE NCBC and OOI HYS11

We download the east-component seismograms of the NEPTUNE station NCBC and the OOI station HYS11 for 27 ISC cataloged high-quality *T*-wave events around the Fox islands, bandpass filter the waveforms to 3-5 Hz, calculate the envelopes with a 5-s sliding smooth window, and compute the HYS11/NCBC peak amplitude ratios within a 150-s window after the predicted *T*-wave arrival times (Figure S5). The ISC body wave magnitude mb is converted to moment magnitude Mw using the empirical equation $M_w = (m_b^{ISC} - 1.65)/0.65$ (Das et al., 2011).

The HYS11/NCBC amplitude ratios have a mean number of 0.35 with a standard deviation of 0.07 (Figure S5). The consistent ratios indicate that T-waves at HYS11 and NCBC from earthquakes near the Fox islands share similar propagation effects, that allows us to use NCBC as a reference to synthesize T-wave at HYS11 from the Mw5.2 Fox island earthquake. The procedure works as follows: we download the HYS11 east-component seismograms of seven Mw5.3-5.9 earthquakes in this region (Figure S6); For each event, the corresponding T-wave is calibrated to Mw5.2 by scaling its own peak amplitude to $A_{HYS11}^{Mw5.2} = A_{NCBC}^{Mw5.2} * 0.35$, where $A_{NCBC}^{Mw5.2}$ is the observed NCBC T-wave peak amplitude from the Mw5.2 Fox Island event; Once the Mw5.2 T-waves at HYS11 are available, we can follow the same approach as that for the OOI North but use the seven Mw5.2 T-waves to conduct the SOT robustness analysis for HYS11 .

**Text S4. Correlation between the variations of OBDAS noise level and ocean dynamics**

We download wind significant wave height, wind speed, and wind direction data for the OOI OBDAS region from Copernicus Climate Change Service (C3S) Climate Data Store (CDS; DOI:10.24381/cds.adbb2d47). These parameters are commonly used to characterize the ocean swells and locally generated surface gravity waves. Notably, we observed substantial shifts in the ocean state over the course of the 4-day experiment (Figure S7). In particular, a sudden change in wind direction and significant wave height was recorded on November 4th, 2021, coinciding with the initiation of the increase in OBDAS noise level on the same date.

**Text S5. Influence of OBDAS noise level on its performance for SOT**

We randomly select 20 noise samples from the first 24 hours and another 20 noise samples for the last 24 hours, representing low and high noise levels, respectively. We generate 190 pseudo-repeating pairs for each testing earthquake magnitude in each noise level scenario and compute the corresponding SOT robustness and cross-correlation amplitude peaks. It is clear that the high noise level results in deterioration in SOT performance (Figure S8).

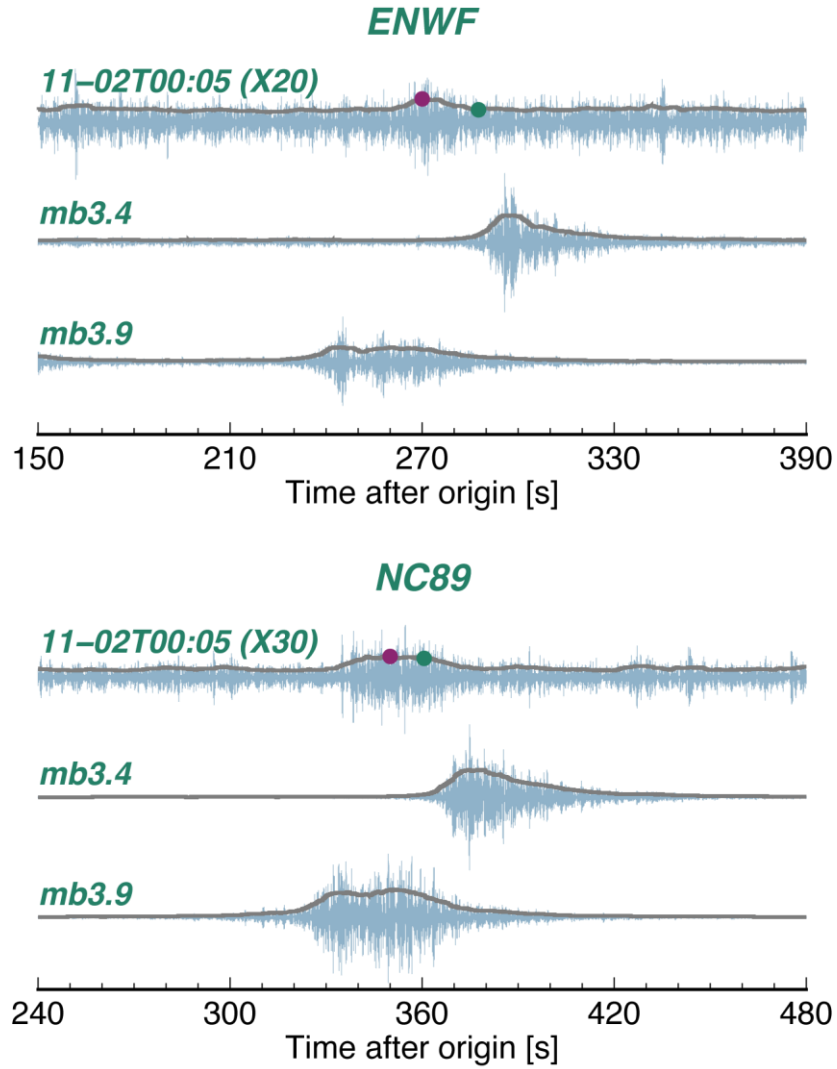**Text S6. Testing different noise percentile thresholds for the stochastic removal**

Following the method used in Figure 11a, we randomly select 20 noise windows and generate 190 pseudo-repeating OBDAS pairs for different earthquake magnitudes ranging from M2.7 to M4.1. For each magnitude, we test six different noise thresholds from 50th percentile to 100th percentile of selected noise for the stochastic removal. After the curvelet denoising, we conduct the SOT measuring for each repeating pair and examine the time shift retrieval. Overall, using the six noise thresholds yields comparable SOT performance, in terms of SOT robustness, across the tested earthquake magnitude range (Figure S9).
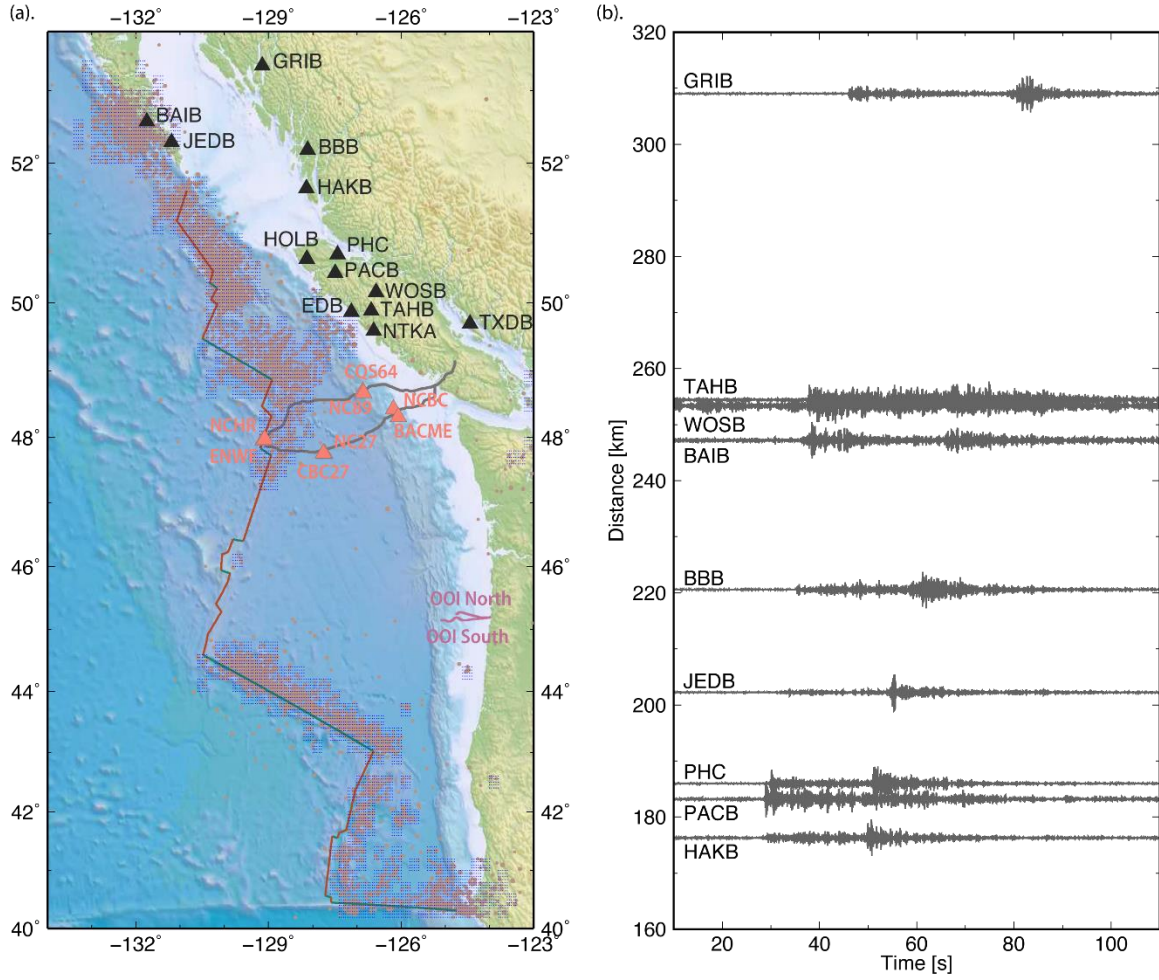
Figure S1. (a). Map of background seismicity (dark gray circles), grid-search locations (blue dots) and seismic stations used for locating earthquakes. Black triangles are land stations of which clear *P*-waves and *S*-waves are observed and used for locating earthquakes. (b). An example of *P*-waves and *S*-waves (5-10 Hz) recorded at onshore stations from Event No.11 in Table S1.
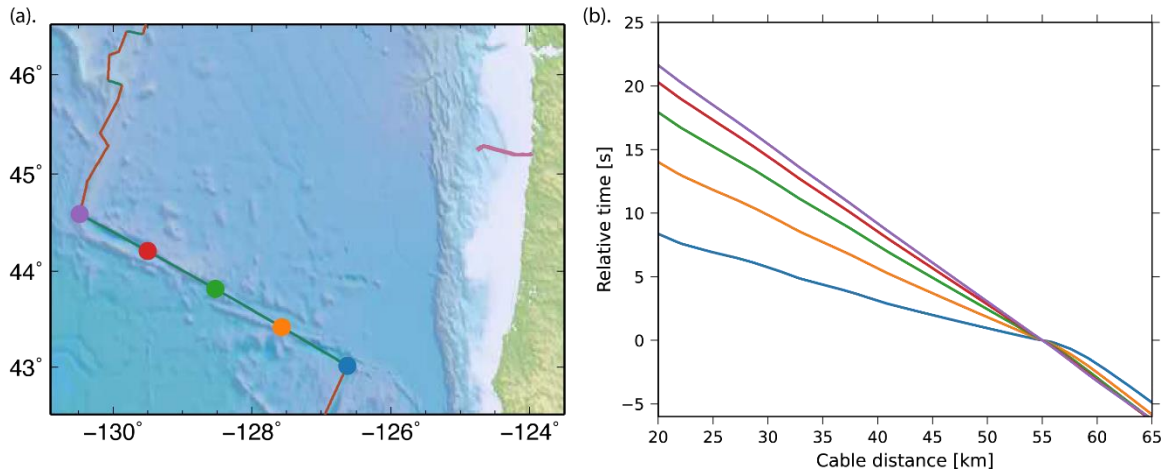
Figure S2. OOI North *T*-wave slowness sensitivity to earthquake location. (a). Map view of five equally spaced Blanco earthquake testing locations and the OOI North OBDAS. (b). Theoretical *T*-wave arrival times on OOI North, relative to that at a cable distance of 55km. Each line shows the arrival times of corresponding testing location in (a). Note the arrival time kinks around 55 km due to a cable geometry change.

ENWF

11–02T00:05 (X20)

mb3.4

mb3.9

150   210   270   330   390
Time after origin [s]

NC89

11–02T00:05 (X30)

mb3.4

mb3.9

240   300   360   420   480
Time after origin [s]

Figure S3. *T*-waves observed at two NEPTUNE stations from the 11-02T00:05 Blanco earthquake and two Blanco events (mb3.9 & mb3.4) occurred in 2021-11-01 as shown in Figure 13. The waveforms are bandpass filtered between 4-8 Hz, the gray lines and green dots represent the corresponding envelopes and predicted *T*-wave arrival times from the estimated location of the 11-20T00:05 event in Figure 9, respectively. It is hard to identify *T*-waves at other NEPTUNE stations due to their high noise levels.
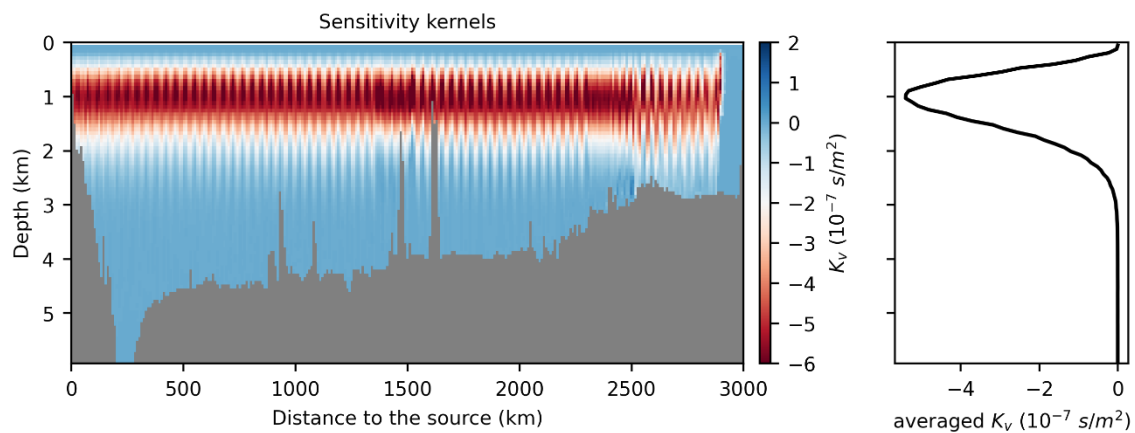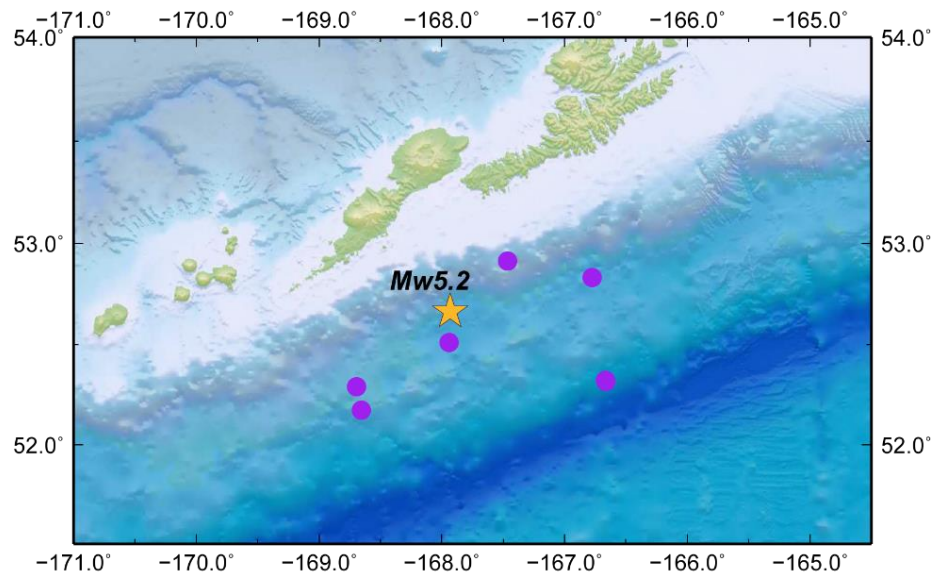
Figure S4. *T*-wave travel time sensitivity kernel (2.5-3.5 Hz) for the Aleutian-OOI path. The right panel is the averaged *T*-wave sensitivity kernel along the path.
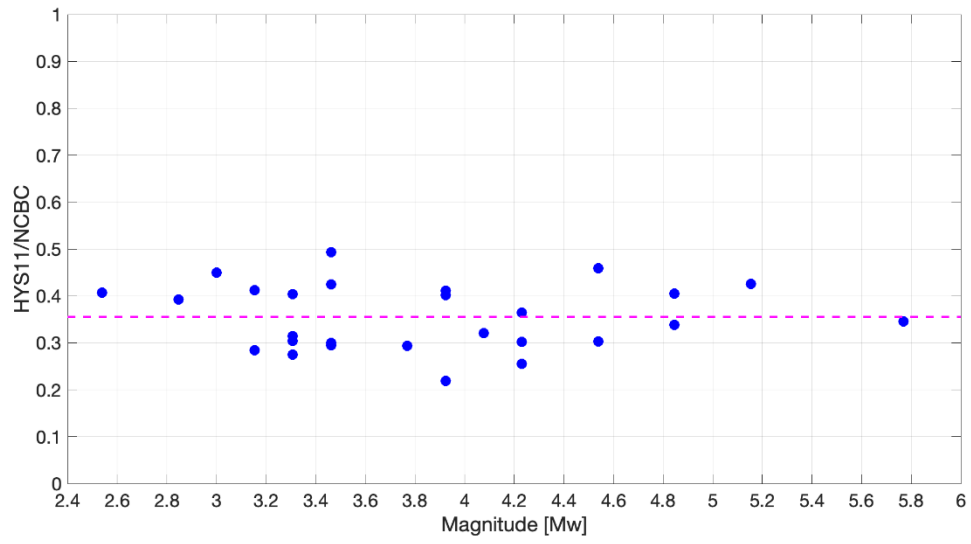
Figure S5. Amplitude ratios of *T*-wave envelopes between OOI HYS11 and NEPTUNE NCBC for ISC catalogued earthquakes near the Fox Islands. The dashed line is the averaged ratio (~0.35) among all the data points.
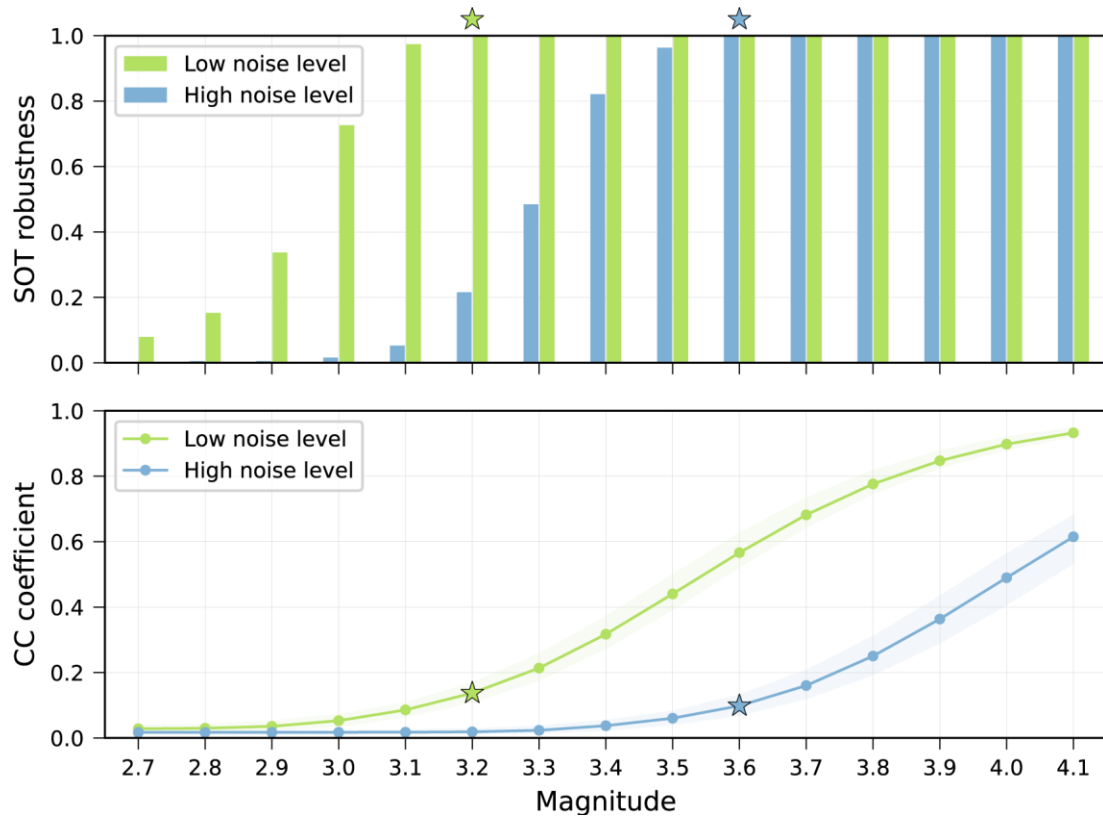
Figure S6. Seven moderate size events (purple circles) used in calculating the SOT robustness of HYS11. It is noted that the locations of two events overlap, making them visually hard to distinguish.
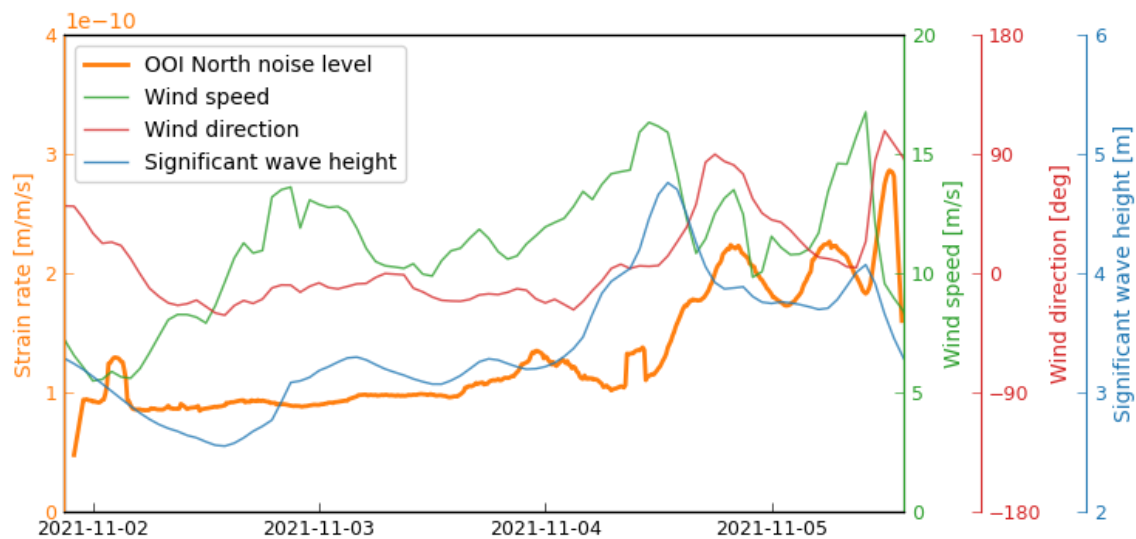
Figure S7. Comparison of OBDAS noise level, wind speed (at 10 m above the sea surface), wind direction and significant wave height.

Figure S8. Noise effect on OBDAS performance for SOT. (a). Comparison of SOT robustness between low noise level scenario and high noise level scenario for denoised OOI North OBDAS data. (b). Corresponding cross-correlation amplitude between low noise level and high noise level on OBDAS. The stars mark the minimum magnitudes that yield reliable time shift measurements.
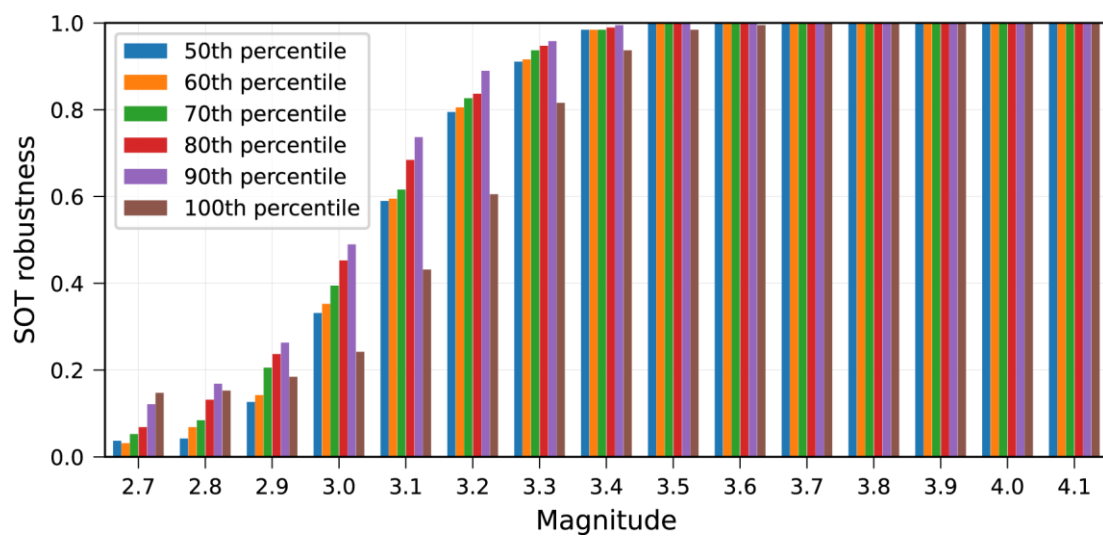
Figure S9. Effects of noise threshold in stochastic removal on the OBDAS performance for SOT.
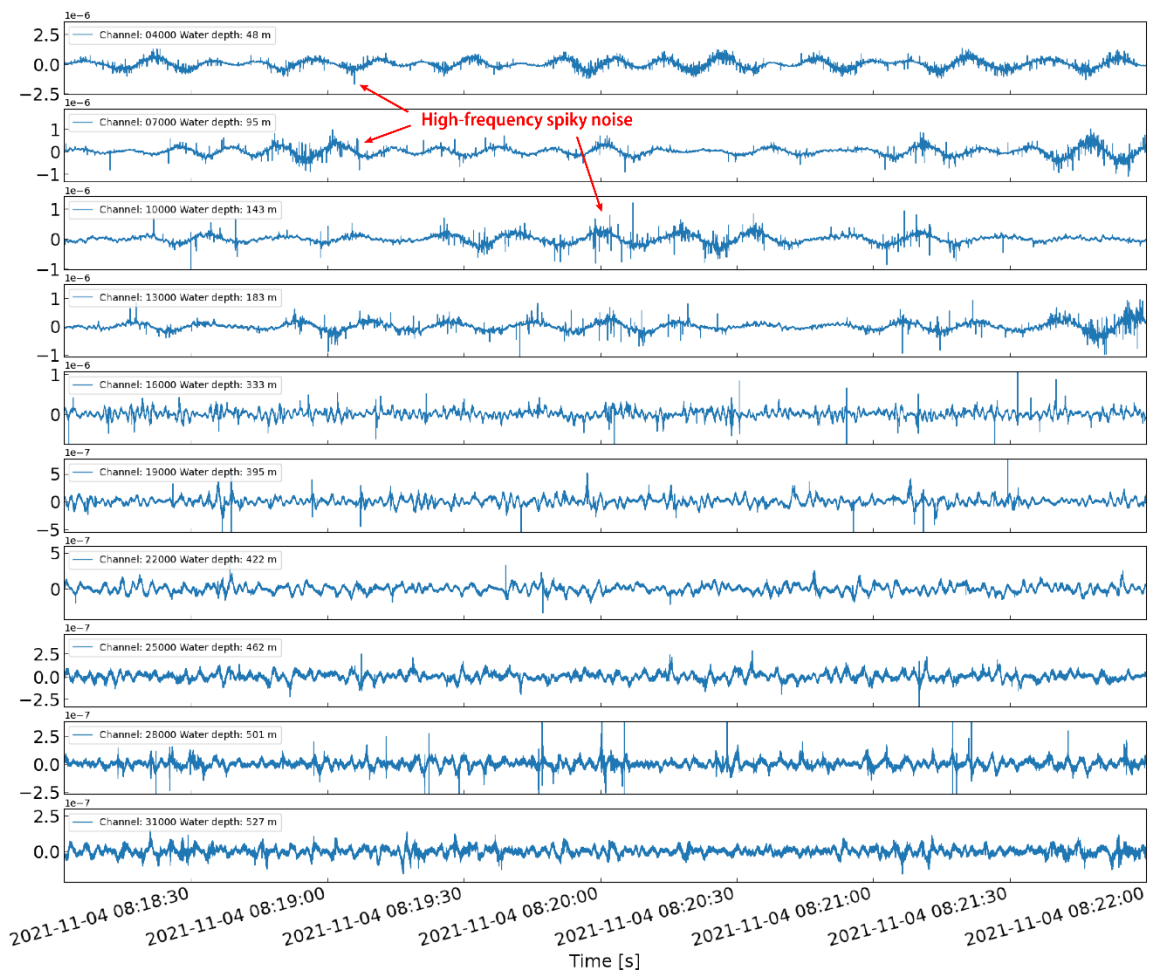
Figure S10. 4-min raw strain rate waveforms recorded at OOI North. The channel index is indicated at the top left. Strong high-frequency noises emerge at the peaks and troughs of ocean gravity waves. These noises become weaker in channels at larger ocean depths. Note that the y-axis has a different scale in each subplot.

No.	Event time (UTC)	Latitude	Longitude	Depth [km]	Magnitude	Data used for location
1	2021-11-01 22:59:13.64	47.20°	-129.20°	10.0*	--	*T*-wave
2	2021-11-01 23:19:59.70	49.16°	-128.32°	10.0*	ML1.6	*P*-, *S*-waves
3	**2021-11-02 00:11:12.64**	**43.90°**	**-129.55°**	**10.0***	**--**	***T*-wave**
4	**2021-11-02 02:14:38.88**	**50.24°**	**-129.82°**	**10.0***	**ML2.3**	***P*-, *S*-waves**
5	**2021-11-02 05:41:35.24**	**50.40°**	**-129.78°**	**10.0***	**ML1.7**	***P*-, *S*-waves**
6	**2021-11-02 08:47:56.82**	**47.85°**	**-128.90°**	**10.0***	**--**	***T*-wave**
7	**2021-11-02 12:02:44.29**	**43.35°**	**-127.10°**	**10.0***	**--**	***T*-wave**
8	2021-11-02 13:13:46.84	47.75°	-128.60°	10.0*	--	*T*-wave
9	**2021-11-02 15:01:05.13**	**47.20°**	**-129.20°**	**10.0***	**--**	***T*-wave**
10	2021-11-02 18:01:17.36	49.17°	-128.00°	10.0*	MLSn2.0	ISC catalog
11	**2021-11-02 18:15:17.79**	**50.49°**	**-130.16°**	**10.0***	**MLSn2.5**	**ISC catalog**
12	2021-11-03 00:24:50.73	40.35°	-124.28°	27.5	Mw4.4	ISC catalog
13	2021-11-03 03:33:51.87	49.08°	-128.06°	10.0*	ML1.8	*P*-, *S*-waves
14	**2021-11-03 15:43:07.68**	**47.80°**	**-129.40°**	**10.0***	**--**	***T*-wave**
15	**2021-11-03 16:20:18.26**	**47.75°**	**-128.90°**	**10.0***	**--**	***T*-wave**
16	2021-11-04 01:59:52.31	47.45°	-128.65°	10.0*	--	*T*-wave
17	**2021-11-04 03:43:21.34**	**44.20°**	**-129.05°**	**10.0***	**--**	***T*-wave**
18	2021-11-04 05:15:01.55	48.65°	-128.35°	10.0*	--	*T*-wave
19	**2021-11-04 05:48:50.15**	**44.40°**	**-129.20°**	**10.0***	**--**	***T*-wave**
20	**2021-11-04 08:57:06.93**	**52.67°**	**-167.93°**	**39.3**	**Mw5.2**	**ISC catalog**

21	2021-11-04 10:23:49.43	47.85°	-128.55°	10.0*	--	*T*-wave
22	**2021-11-04 14:38:35.49**	**44.70°**	**-129.05°**	**10.0***	**--**	***T*-wave**
23	**2021-11-04 19:17:15.98**	**54.73°**	**-156.92°**	**10.0**	**mb4.5**	**ISC catalog**
24	2021-11-04 20:16:14.48	47.20°	-128.80°	10.0*	--	*T*-wave
25	**2021-11-04 20:32:16.45**	**43.60°**	**-128.90°**	**10.0***	**--**	***T*-wave**
26	**2021-11-04 23:39:17.62**	**54.69°**	**-156.91°**	**10.0**	**mb4.0**	**ISC catalog**
27	**2021-11-05 05:12:49.48**	**43.60°**	**-128.40°**	**10.0***	**--**	***T*-wave**

Table S1. *T*-wave catalog during the OOI DAS experiment using the NEPTUNE array. Symbol * denotes that the depth is fixed at 10 km. Earthquakes highlighted in red bold font generate identified *T*-waves on OOI DAS.